Ternary Group VIII Hydrides: Ligand Field and Cation Orbital Effects in Their Electronic Structures

Gordon J. Miller,[*,†] Haibin Deng,[‡] and Roald Hoffmann[‡]

Departments of Chemistry, Iowa State University, Ames, Iowa 50011, and Cornell University, Ithaca, New York 14853

The electronic structure and bonding of some recently discovered ternary hydrides with group VIII metals are evaluated using tight-binding extended Hückel band structure calculations. Various computational tools that include charge iteration of the transition metal orbital parameters, Mulliken population analyses, and second moment scaling methods were utilized to examine the bonding in Mg_2RuH_4 and Mg_3RuH_3. Our results indicate that the unusual sawhorse geometry of the d^8 RuH_4 fragment in Mg_2RuH_4 is preferred over a square planar configuration due to zeroth-order ligand field effects, oxidation state at the transition metal, and metal–metal bonding between adjacent fragments. In the extraordinary structure of Mg_3RuH_3, Mg valence orbitals are actively involved in chemical bonding and contribute to the stability of the unusual electron count at Ru.

Hydrogen combines with many metals to form binary hydrides that range from insulators to metals and even superconductors.[1] The group VIII metals (Fe–Os, Co–Ir, Ni–Pt), however, generally do not form thermodynamically stable binary hydrides, the notable exception to this list being palladium.[2] Nevertheless, during the past two decades, numerous ternary hydrides and deuterides, A_xMH_y (A = alkali or alkaline earth metal; M = group VIII element), have been established.[3] Examples include Mg_2FeD_6,[4] Mg_2CoD_5,[5] Mg_2NiD_4,[6] and Na_2PtH_4.[7] With applications toward potential hydrogen storage devices, these classes of compounds offer extremely high hydrogen content per unit volume and weight, but with relatively strong metal–hydrogen bonds,[2b] which is not conducive to hydrogen storage.

Electronic structure calculations on some of these ternary systems have been performed to give an accurate description of the metal–hydrogen bond in order to learn how it could be weakened.[8a] These results have confirmed the application of classical electron-counting rules to these complexes.[9] The series $Mg_2(Fe, Co, Ni)H_y$ (y = 6, 5, 4, respectively) contains isolated $[MH_y]^{4-}$ fragments that obey the 18-electron rule,[4–6] while Na_2-

PtH_4 displays square planar $[PtH_4]^{2-}$ units,[7] which are appropriate for d^8 16-electron transition metal complexes. Recent synthetic efforts in the Mg–Ru–H system uncovered seemingly surprising coordination geometries for the Ru atoms. For example, in Mg_2-RuH_4,[10] formally d^8 $[RuH_4]^{4-}$ moieties adopt the sawhorse configuration.[11] These complexes are interconnected to form zigzag chains of Ru atoms separated by a distance of 3.236 Å, as shown in structure 1. However, in the stoichiometric analogue,

1   2
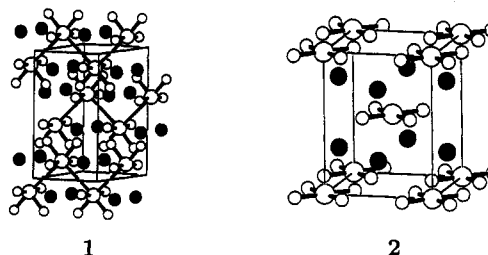
Na_2PtH_4, square planar $[PtH_4]^{2-}$ complexes are isolated from each other[7] (see structure 2). Another compound, Mg_3RuD_3, contains T-shaped RuH_3 units linked via a Ru–Ru contact of 3.310 Å[12] (cf. 3).

3
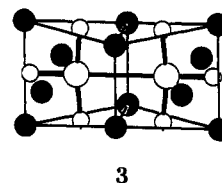
Our convention in these diagrams is to represent the cations (Mg or Na) by darkened circles, the transition metal (Ru or Pt) by large open circles, and hydrogen by small open circles.

These systems (1–3) clearly provide a strong bridge between molecular and solid-state hydrides. What accounts for the stability of these "unusual" transition metal hydride fragments in these ternary systems? What role does metal–metal bonding

† Iowa State University.
‡ Cornell University.
● Abstract published in *Advance ACS Abstracts*, March 1, 1994.
(1) *Hydrogen in Metals I*; Alefeld, G., Völkl, J., Eds.; Topics in Applied Physics, Vol. 28; Springer-Verlag: Heidelberg, Germany, 1978.
(2) (a) Speiser, R. In *Metal Hydrides*; Müller, W. M., Blackledge, J. P., Libowitz, G. G., Eds.; Academic Press: New York, 1968; p 51. (b) Griessen, R.; Riesterer, T. In *Hydrogen in Intermetallic Compounds I*; Schlapbach, L., Ed.; Topics in Applied Physics, Vol. 63; Springer-Verlag: Heidelberg, Germany, 1988; p 219.
(3) (a) Yvon, K.; Fischer, P. In *Hydrogen in Intermetallic Compounds I*; Schlapbach, L., Ed.; Topics in Applied Physics, Vol. 63; Springer-Verlag: Heidelberg, Germany, 1988; p 87. (b) Bronger, W. *Angew. Chem., Int. Ed. Engl.* 1991, 30, 759.
(4) (a) Didisheim, J.-J.; Zolliker, P.; Yvon, K.; Fischer, P.; Schefer, J.; Gubelmann, M.; Williams, A. F. *Inorg. Chem.* 1984, 23, 1953. (b) Didisheim, J.-J.; Yvon, K.; Fischer, P.; Schefer, J.; Gubelmann, M.; Williams, A. F. *Z. Kristallogr.* 1983, 162, 61.
(5) Zolliker, P.; Yvon, K.; Fischer, P.; Schefer, J. *Inorg. Chem.* 1985, 24, 4177.
(6) Noréus, D.; Werner, P.-E. *J. Less-Common Met.* 1984, 97, 215. (b) Zolliker, P.; Yvon, K.; Jorgensen, J. D.; Rotella, F. *Inorg. Chem.* 1986, 25, 3590.
(7) Bronger, W.; Müller, P.; Schmitz, D.; Spittank, H. *Z. Anorg. Allg. Chem.* 1984, 516, 35.
(8) (a) Gupta, M.; Schlapbach, L. In *Hydrogen in Intermetallic Compounds I*; Schlapbach, L., Ed.; Topics in Applied Physics, Vol. 63; Springer-Verlag: Heidelberg, Germany, 1988; p 139. (b) Lindberg, P.; Noréus, D.; Blomberg, M. R. A.; Siegbahn, P. E. M. *J. Chem. Phys.* 1986, 85, 4530.
(9) Albright, T. A.; Burdett, J. K.; Whangbo, M.-H. *Orbital Interactions in Chemistry*; Wiley-Interscience: New York, 1985.

(10) Bonhomme, F.; Yvon, K.; Triscone, G.; Jansen, G.; Auffermann, G.; Müller, P.; Bronger, W.; Fischer, P. *J. Alloys Comp.* 1992, 178, 161.
(11) Four-coordinate *sawhorse* geometries are also called *angular, butterfly*, and *cis*-divacant. The geometry is derived from an octahedral RuH_6 complex by removing two *cis* ligands.
(12) Bonhomme, F.; Yvon, K.; Fischer, P. *J. Alloys Comp.* 1992, 186, 309.

play, and how do the electropositive cations influence the chemical bonding in these species? This paper will examine the questions using the extended Hückel method[13] to determine the electronic structure of some of these intriguing systems. Details of the method are outlined in the Appendix. In particular, we shall probe examples whose transition metals adopt electronic configurations of d^8 counts and beyond.

Mg₂RuH₄ vs Na₂PtH₄

As similar as Mg_2RuH_4 and Na_2PtH_4 "appear" at first glance, it is somewhat surprising that their structures should show such extreme differences (see **1** and **2**). Although each transition metal formally adopts a d^8 configuration, their different formal oxidation states, Ru(0) and Pt(II), greatly influence the observed coordination geometries. Furthermore, a Ru–Ru separation of 3.236 Å indicates some degree of metal–metal bonding (Pauling bond order[14] is 0.06), which is completely absent between Pt atoms in Na_2PtH_4. When we include the cations, these two structures could serve as "solid-state isomers" of one another.[15] The electropositive Na or Mg atoms form a slightly distorted simple cubic framework, and Pt or Ru occupy half of the cubic centers; i.e., these structures represent alternative defect-CsCl arrangements.[16] Pt atoms occupy sites that maximize their mutual internuclear separations while Ru atoms form zigzag chains. There is certainly a synergistic relationship between the spatial distribution of the transition metal atoms within the electropositive matrix and the local coordination of these metals by hydrogen.

Previous theoretical investigations on these two d^8 geometries indicated that the D_{4h} square planar ML₄ fragment would be energetically preferred over the C_{2v} sawhorse arrangement for electronegative metals M and strong σ-donor ligands L.[17] Since valence-state ionization potentials increase as the oxidation state of an element increases,[18] so does that metal's electronegativity. Therefore, d^8 metals in positive oxidation states, like Rh(I) and Pt(II), adopt square planar structures. On the other hand, Ru-(0) and Os(0) exhibit the sawhorse geometry with four CO ligands, but also with metal–metal bonding in the triangular $[Ru(CO)_4]_3$ and $[Os(CO)_4]_3$ species.[19] In addition, $Fe(CO)_4$ is a paramagnetic monomer whose structure lies between tetrahedral and sawhorse arrangements.[20] In a previous paper one of us in fact suggested that there might exist an alternative to the three-membered ring, single-bonded $[M(CO)_4]_3$ structure, namely an extended quasi-finite zigzag chain.[17] This is precisely the atomic arrangement of the RuH₄ substructure in Mg_2RuH_4. However, in Mg_2RuH_4, the Ru–Ru distance of 3.236 Å is significantly greater than 2.84 Å found in $Ru_3(CO)_{12}$. Furthermore, Madelung calculations[21] performed on $(Mg^{2+})_2Ru^0(H^-)_4$ in both the Mg_2RuH_4 and Na_2-PtH_4 modifications at equal unit cell volumes favor the square planar system by 1.7 eV per formula unit. And, finally, summation of orbitals energies of MH₄ fragments (M = Ru or Pt) show that the d^8 square planar geometry is always preferred by nearly 2.0 eV over the sawhorse coordination.

We shall first address the role played by metal–metal bonding in the Mg_2RuH_4 structure. To do this, we examined a sequence

of hypothetical structures, which are shown in Figure 1. The two basic "monomer" structures are the **Ia** sawhorse unit and the **IIa** square planar structure. These can interact as "dimers," **Ib** and **IIb**, "trimers," **Ic** and **IIc**, "tetramers," **Id** and **IId**, and the infinite chains **Ie** and **IIe**. Table 1 lists computational results on various $[RuH_4]_n^{4n-}$ aggregates as well as both actual and hypothetical A_2MH_4 structure types (for purposes of these calculations, A = Mg, M = Ru). Clearly, electronic energies indicate that the sawhorse geometry is stabilized by Ru–Ru bonding. Within the set of model $[RuH_4]_n^{4n-}$ structures, **Ia–Ie**, the greatest effects occur for $n \geq 3$. Molecular orbital (MO) energy diagrams illustrated in Figure 2 for the $n = 2$ and $n = 3$ cases provide a transparent understanding of the stabilization due to Ru–Ru bonding.

Let us analyze the monomer units and their oligomers. The fragment MO's of a C_{2v} sawhorse RuH₄ unit in **4** show the three-below-two pattern of the parent octahedral complex. The three

4
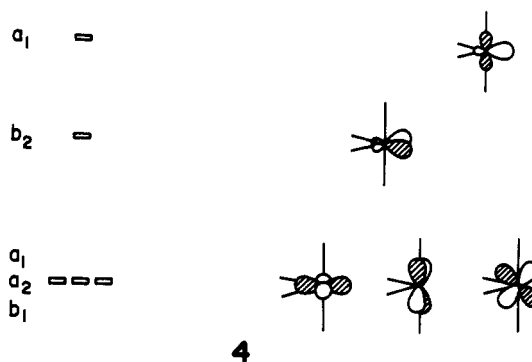
degenerate orbitals at lower energy are Ru–H σ nonbonding, and the two orbitals at higher energies are Ru–H σ antibonding (d(Ru–H) = 1.70 Å). The b₂ frontier orbital, which is a mixture of xy and x character within our coordinate system, lies approximately 1.0 eV lower than the a₁ orbital, which is largely z^2 with some s and y contributions.

Upon formation of the dimer **Ib** (d(Ru–Ru) = 3.236 Å as in Mg_2RuH_4), the b₂ frontier orbitals interact to give $\pi(b_{2u})$ and $\pi^*(b_{1g})$ MO's, while the a₁ frontier levels combine into $\sigma(a_g)$ and $\sigma^*(b_{3u})$ MO's (see Figure 2). The relatively weak through-space π overlap between the b₂ levels ($S = 0.056$) leads to a small π–π^* energy difference of 0.56 eV and keeps $\pi^*(b_{1g})$ below $\sigma(a_g)$. Since $\pi^*(b_{1g})$ is the highest occupied MO (HOMO), a negligible stabilization energy relative to the monomer as well as the weak, but slightly bonding, Ru–Ru overlap population results (see Table 1). Hybridization with the valence x orbitals of Ru produces the positive values for these two quantities.

In the triangular cluster **Ic**, $[Ru_3H_{12}]^{12-}$, the linear combinations of b₂ frontier orbitals form a Möbius system (**5**; two-below-one), while those of the a₁ levels form a Hückel system (**6**; one-below-two).[22] The difference in the pattern of MO energies lies in the

5

6
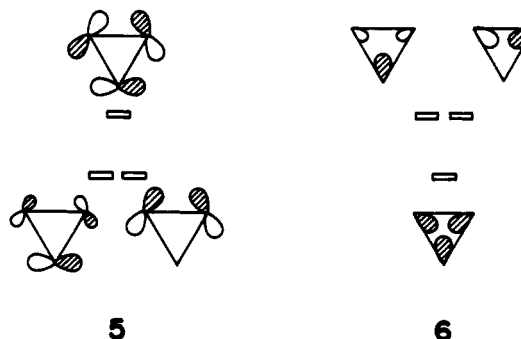
head-to-tail overlap between adjacent b₂ orbitals (Möbius) but head-to-head overlap between a₁ orbitals (Hückel). Due to the

(13) Hoffmann, R. *J. Chem. Phys.* **1963**, *39*, 1397.
(14) Pauling's expression is $D(n') = D_1 - 0.6 \log n'$ with n' = bond order. See: Pauling, L. *The Nature of the Chemical Bond*; Cornell University Press: Ithaca, NY, 1960; p 255.
(15) von Schnering, H. G.; Hönle, W. *Chem. Rev.* **1988**, *88*, 243.
(16) Hyde, B. G.; Andersson, S. *Inorganic Crystal Structures*; Wiley-Interscience: New York, 1989.
(17) Hoffmann, R.; Minot, C.; Gray, H. B. *J. Am. Chem. Soc.* **1984**, *106*, 2001.
(18) Ballhausen, C. J.; Gray, H. B. *Molecular Orbital Theory*; W. A. Benjamin: New York, 1964; p 120.
(19) Ru₃(CO)₁₂: Mason, R.; Rae, A. I. M. *J. Chem. Soc. A* **1978**, 778. Os₃(CO)₁₂: Corey, E. R.; Dahl, L. F. *Inorg. Chem.* **1962**, *1*, 521.
(20) Davies, B.; McNeish, A.; Poliakoff, M.; Turner, J. J. *J. Am. Chem. Soc.* **1977**, *99*, 7573.
(21) Madelung terms were evaluated using the Ewald method: Ziman, J. M. *Principles in the Theory of Solids*; Cambridge University Press: Cambridge, U.K., 1964; p 39.
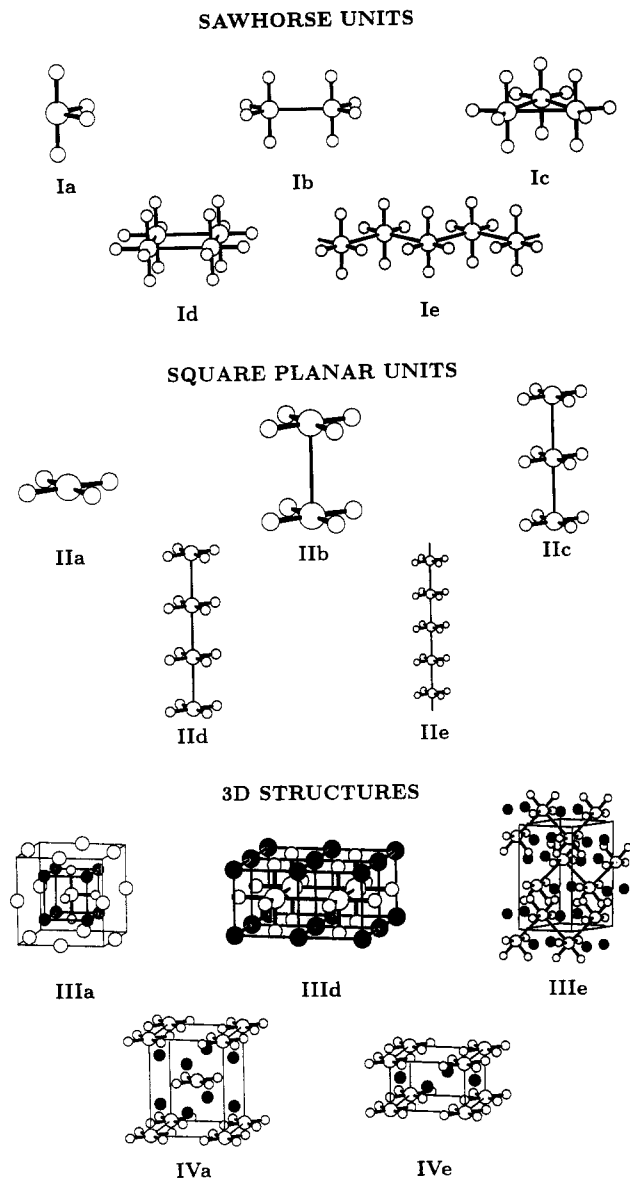
SAWHORSE UNITS

Ia   Ib   Ic

Id   Ie

SQUARE PLANAR UNITS

IIa   IIb   IIc

IId   IIe

3D STRUCTURES

IIIa   IIId   IIIe

IVa   IVe

Figure 1. Structural models listed in Table 1. Small shaded circles are Mg and Na; large open circles are Ru and Pt; small open circles are H.

Table 1. Computational Results from Structures Containing the Sawhorse (C_{2v}; I and III) or Square Planar (D_{4h}; II and IV) RuH$_4$ Fragment[a]

system	structure	energy (eV)	q(Ru)	p(Ru–Ru)
Isolated Hypothetical Fragments				
Sawhorse				
[RuH$_4$]$^{4-}$	Ia	0.00	9.487	
[RuH$_4$]$_2^{8-}$	Ib	–0.03	9.484	0.025
[RuH$_4$]$_3^{12-}$	Ic	–0.15	9.473	0.196
[RuH$_4$]$_4^{16-}$	Id	–0.22	9.475	0.189
$^1_\infty$[RuH$_4$]$^{4-}$	Ie	–0.19	9.488	0.131
Square Planar				
[RuH$_4$]$^{4-}$	IIa	–2.15	9.591	
[RuH$_4$]$_2^{8-}$	IIb	–2.12	9.589	0.022
[RuH$_4$]$_3^{12-}$	IIc	–2.10	9.588	0.020
[RuH$_4$]$_4^{16-}$	IId	–2.10	9.589	0.021
$^1_\infty$[RuH$_4$]$^{4-}$	IIe	–2.08	9.586	–0.009
Mg$_2$RuH$_4$ Models				
Sawhorse				
antifluorite	IIIa	0.00	8.350	
square cluster	IIId	–0.88	8.441	0.058
Mg$_2$RuH$_4$-type	IIIe	–0.79	8.444	0.051
Square Planar				
Na$_2$PtH$_4$-type	IVa	–1.73	8.682	
K$_2$PtCl$_4$-type	IVe	–1.62	8.673	–0.006

[a] The energy values are total energies per formula unit as referenced to either the isolated sawhorse fragment **Ia** or structure **IIIa**. q(Ru) is the Mulliken population for the Ru centers. p(Ru–Ru) is the overlap population between Ru centers, when appropriate. Structures are illustrated in Figure 1.

strength of the three-center orbital overlaps and the different irreducible representations spanned by the highest energy Möbius (a$_2'$; Ru–Ru antibonding) and lowest energy Hückel (a$_1'$; Ru–Ru bonding) levels, these combinations of b$_2$ and a$_1$ frontier orbitals do not mix, and the bonding a$_1'$ level becomes the HOMO. Thus, we find a greater stabilization energy for the trimer **Ic** and a significant increase in the Ru–Ru overlap population over that of the dimer **Ib**. This trend continues for larger ring systems, and the tetramer **Id** (square geometry) shows the lowest total energy per formula unit.

The total energy of the quasi-infinite one-dimensional zigzag chain of C_{2v}-RuH$_4$ fragments **Ie** lies between those of the tetramer **Id** and the trimer **Ic**, but the Ru–Ru overlap population drops significantly in value. Symmetry characteristics of the energy bands, shown in Figure 3, indicate that dispersion effects account for the lower Ru–Ru overlap population, although the through-space σ overlap of b$_2$ orbitals in the zigzag chain **Ie** ($\angle$(Ru–Ru–Ru) = 95.8°) is greater than that in the trimer **Ic** ($\angle$(Ru–Ru–Ru) = 60.0°) and only slightly smaller than that in the tetramer **Id** ($\angle$(Ru–Ru–Ru) = 90.0°). Let us analyze these effects in some detail.

Symmetry operations of the zigzag chain that maintain the invariance of the wavevector **k** (**k** is parallel to **c*** in Mg$_2$RuH$_4$) include the horizontal (yz) mirror plane of the chain and the

vertical (xz) glide plane, which transforms one RuH$_4$ fragment into an adjacent site. Since the frontier orbitals, b$_2$ and a$_1$, are both symmetric with respect to the horizontal mirror plane, the discriminating operation is the glide plane, which also dictates that degeneracies occur at the zone edge.[23] Only at the zone center Γ (**k** = 0) and the zone edge Z (**k** = π**c*** = (π/c)**z**) can the inversion center (located between adjacent Ru atoms) be included as a symmetry operation. At the Γ point, the group of the wavevector is isomorphous with D_{2h}, and the four crystal orbitals arising from combinations of b$_2$ and a$_1$ each adopt different irreducible representations (see Figure 3). The two Ru–Ru bondind bands (b$_{3g}$ and a$_g$) lie lower in energy than the two Ru–Ru antibonding bands (b$_{1u}$ and b$_{2u}$). Dispersion effects tend to bring the bonding and antibonding combinations of the b$_2$ (b$_{3g}$ and b$_{1u}$) and a$_1$ (a$_g$ and b$_{2u}$) bands together at the zone edge to form Ru–Ru nonbonding levels. However, at points away from Γ, the nodal characteristics of these fragment orbitals lead to identical irreducible representations for the antibonding combination of b$_2$ and the bonding combination of a$_1$ orbitals: they are both antisymmetric with respect to the xz glide plane. Therefore, a strong symmetry-avoided crossing results, leading to a bandgap between occupied and unoccupied crystal orbitals. In addition, a significant contribution from the antibonding combination of b$_2$ frontier orbitals mixes into the highest occupied band, and the Ru–Ru overlap population in **Ie** becomes slightly reduced from its value for the rings **Ic** and **Id**.

A similar analysis for oligomers of d^8 space planar MH$_4$ fragments **IIa–e** (see Figure 1) reveals that isolated complexes, as found in Na$_2$PtH$_4$, are slightly preferred over any degree of aggregation. This destabilization of oligomeric structures occurs primarily due to the occupation of metal–metal σ-antibonding orbitals that involve mostly z^2 orbitals along the chain.

Clearly, metal–metal bonding is an important component in the electronic structure of Mg$_2$RuH$_4$. Table 1 also lists our results

(22) (a) Walsh, A. D. W. *Trans. Faraday Soc.* **1949**, *45*, 179. (b) Jorgensen, W. L.; Salem, L. *The Organic Chemist's Book of Orbitals*; Academic Press: New York, 1973; pp 22–23. (c) Zimmerman, H. E. *Acc. Chem. Res.* **1971**, *4*, 272.

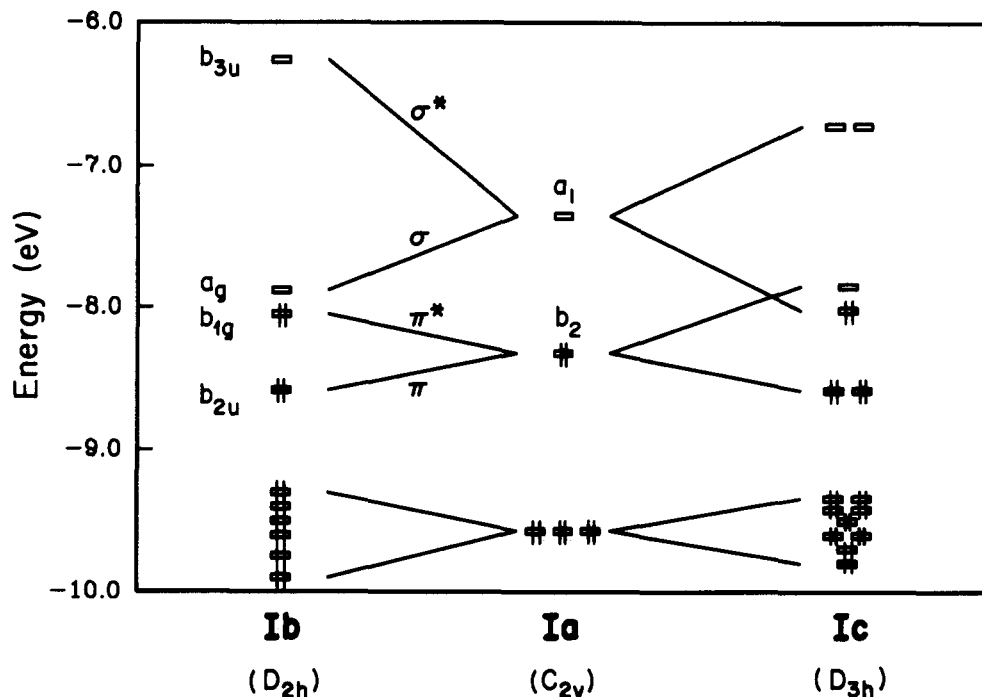(23) Whangbo, M.-H.; Hoffmann, R.; Woodward, R. B. *Proc. Roy. Soc.* **1979**, *A366*, 23.

Figure 2. Molecular orbital (MO) energy level diagrams for the dimeric (**Ib**; left) and trimeric (**Ic**; right) clusters of sawhorse [RuH₄]⁺ fragments (center). Only MO's with largely Ru 4d character are shown. Labels correspond to the D_{2h} and D_{3h} point symmetries of **Ib** and **Ic**, respectively.
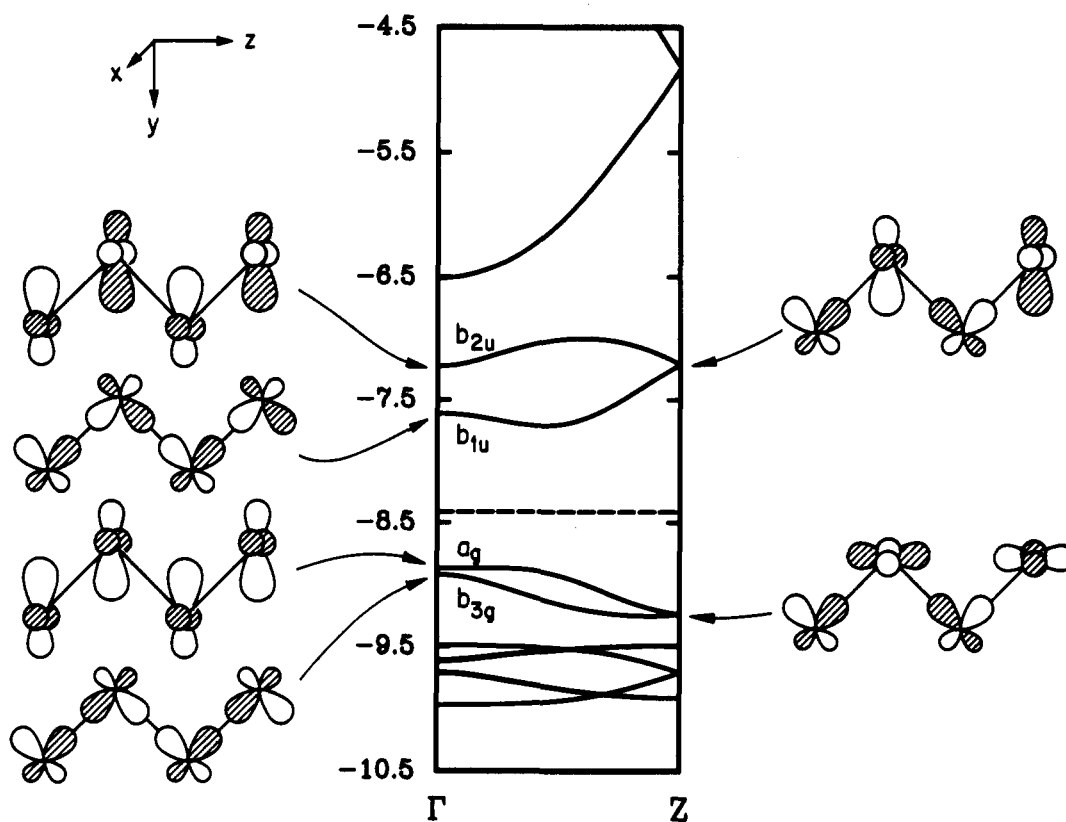

Figure 3. Energy bands of Mg₂RuH₄ along the ΓZ line in the orthorhombic Brillouin zone (parallel to c*). The dashed line at −8.4 eV is the calculated Fermi level. Crystal orbitals at Γ and Z for the highest occupied, b_{3g} and a_g, and lowest unoccupied bands, b_{1u} and b_{2u}, are also depicted.

from calculations on complete three-dimensional models with the same stoichiometry, performed at identical volumes per formula unit (the observed volume in Mg₂RuH₄ is 70.2 Å³). These structures are also shown in Figure 1. Three examples in the table contain RuH₄ sawhorse complexes **IIIa,d,e**, and those showing short Ru–Ru contacts, **IIId,e**, are preferred by 0.88 and 0.79 eV, respectively, over the hypothetical model **IIIa** with no Ru–Ru bonds. **IIIe** is the observed topology of Mg₂RuH₄, whereas

IIId contains square clusters of [RuH₄]₄ units in a cubic array of Mg atoms. On the other hand, structure **IIIa** corresponds to the antifluorite arrangement for the Mg₂Ru framework. Different arrangements of the RuH₄ units in this structure gave energies within 0.03 eV of one another; the average value is reported in Table 1. Note that the energetic preferences for **IIId,e** are approximately 4 times as great as that for **Id,e** over **Ia**, although the Ru–Ru overlap populations are significantly smaller in the
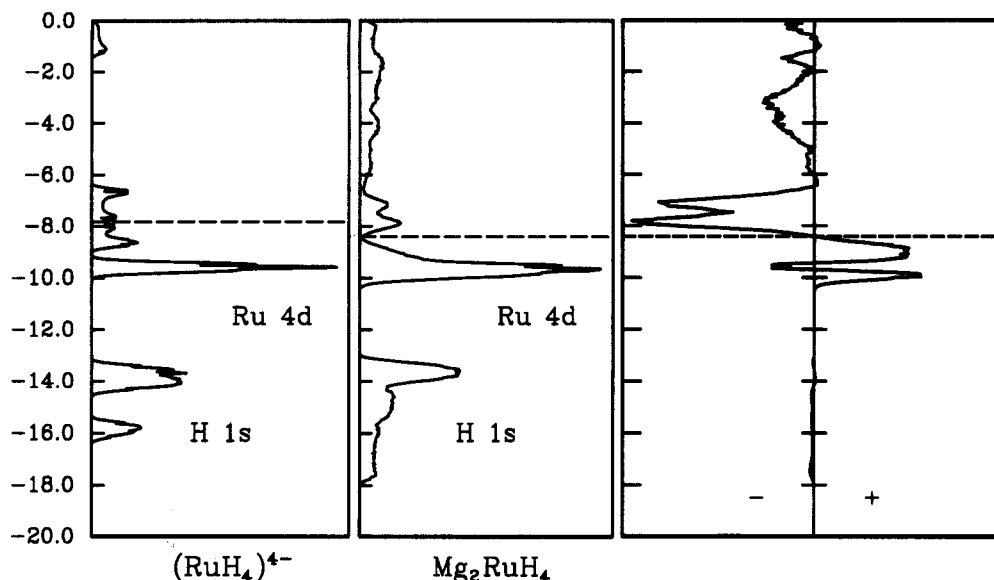
Figure 4. Left and center: Total DOS curves for structure Ie and Mg_2RuH_4 (IIIe). Right: COOP curve for the Ru–Ru interaction in Mg_2RuH_4. Bonding levels occur when the COOP is positive; antibonding, when it is negative. The dashed lines are the calculated Fermi levels for these systems.

Mg_2RuH_4 models. Nevertheless, the crystal orbital overlap population (COOP)[24] curve in Figure 4 indicates that the Ru–Ru bonding is optimized. As the density of states (DOS) curves for both Mg_2RuH_4 (IIIe) and $\frac{1}{\infty}[RuH_4]^{4-}$ (Ie) in the remainder of Figure 4 illustrate, Mg–H orbital overlap considerably enhances the electronic energy of this system by broadening the two narrow hydrogen peaks at –14.0 and –16.0 eV for Ie into a single continuum of orbitals for IIIe between –13.0 and –18.0 eV. Mg orbitals also interact with the highest occupied band of Ie just below –8.0 eV, lowering its energy range to become a shoulder of the strong Ru–H nonbonding orbital peak. The Fermi level also drops when Mg orbitals are introduced. Furthermore, this mixing of Mg 3s and 3p orbitals into the occupied Ru 4d bands leads to the small value of the Ru–Ru overlap population via orbital dilution effects.[25]

The difference in calculated electronic energies for cases IIId,e parallels the slight preference for the square $[RuH_4]_4{}^{16-}$ cluster Id over the zigzag chain Ie. Madelung calculations carried out on these two systems, however, give ionic lattice energies that are 1.55 eV in favor of the chain system IIIe. Therefore, when ionic forces are combined with orbital energies, the observed structure is preferred.

The troubling fact remaining in Table 1, however, is that both metal–metal bonding and cation orbital contributions to the electronic structure are insufficient to counteract the apparently greater ligand field stabilization energy of the square planar geometry for the d^8 configuration. The results of a Mulliken population analysis for the charge on the Ru atoms are also listed in Table 1 (note: charges at Ru equal 8 – q(Ru); Ru is formally in the zero oxidation state for each listing). In general, Ru atoms in the general planar RuH_4 complexes acquire 0.1–0.2 unit of charge more than those in the sawhorse fragments. In order to pursue the origins of this observation, we list in Table 2 the results of a Mulliken population analysis carried out on the two monomeric isomers under different levels of d–s–p hybridization at the Ru site. In all cases the metal atom accumulates greater electron density in the square planar geometry. Since the d-only model reproduces the trend in Table 1, the primary reason stems from the ligand field imposed by the four hydrogen atoms: it is greater in the square planar geometry than in the sawhorse arrangement. Since the square planar HOOMO mixes with Ru

Table 2. Mulliken Population Analysis for $[RuH_4]^{4-}$ Monomers in both the Square Planar and Sawhorse Geometrical Configurations under Various Degrees of d–s–p Hybridization at the Ru Atom

hybridization	square planar	sawhorse	difference
d-only	8.635	8.554	0.081
ds-only	9.097	8.955	0.142
dp-only	9.130	9.121	0.009
total	9.591	9.487	0.104

5s, whereas the sawhorse HOMO mixes with Ru 5p, ds and dp hybridizations counteract each other. Ru 5s mixing increases the Ru population in the square planar complex, and Ru 5p mixing augments that in the sawhorse geometry. Due to the lower energy of the Ru 5s AO relative to the 5p AO's, ds hybridization dominates and enhances the ligand field effect to give greater populations in the square planar geometry.

Recent efforts to expand the effectiveness of the Hückel (tight-binding) approximation led to the development of second-moment scaling.[26] In order to compare various structures and to evaluate their relative stabilities as a function of electron count, this method relies on setting the variance for the different distributions of orbital energies to a fixed value. The variance is related to the second moment of these energy distributions.[27] Applications to a wide spectrum of compounds, which include both molecules and extended solids, indicate that this approach is tremendously successful.[28] For the metal hydride fragments using only 4d orbitals on Ru, there are two energy parameters whose values affect second-moment values. The first is $\Delta(X)$, which is the difference in AO energies between the valence H 1s and Ru 4d orbitals for the particular ligand field with point group X. The other is $\beta(X)$, the 4d–1s resonance integral in the point group X. To compare the two geometries, we devise the following two dimensionless parameters: $\delta \sim \Delta(C_{2v})/\Delta(D_{4h})$ and $\tau \sim \beta(C_{2v})/\beta(D_{4h})$. There remains then one *free* parameter, γ, which relates $\Delta(D_{4h})$ to $\beta(D_{4h})$, i.e., $\Delta(D_{4h}) = \gamma\beta(D_{4h})$.

The graphs in Figure 5 qualitatively illustrate the relative energies of the d^8 sawhorse and square planar geometries as δ and τ vary for various γ values. In each graph, the shaded region indicates where the C_{2v} fragment is preferred. Regardless of the

(24) (a) Hughbanks, T.; Hoffmann, R. *J. Am. Chem. Soc.* **1983**, *105*, 3528. (b) Wijeyesekera, S. D.; Hoffmann, R. *Organometallics* **1984**, *3*, 949.

(25) Orbital dilution refers to lowering of AO coefficients in the MO expression through normalization when additional orbitals occur in the basis set.

(26) (a) Pettifor, D. G.; Podloucky, R. *Phys. Rev. Lett.* **1984**, *53*, 1080. (b) Burdett, J. K.; Lee, S. *J. Am. Chem. Soc.* **1985**, *107*, 3063.

(27) The second moment $\mu_2 \equiv \int E^2 \rho(E)\, dE = \int E^2 \delta(E - E_n)\, dE = \Sigma_n E_n{}^2$, where the summation covers all MO's in the system.

(28) (a) Lee, S. *Acc. Chem. Res.* **1991**, *24*, 249. (b) Lee, S. *J. Am. Chem. Soc.* **1991**, *113*, 101, 8611. (c) Hoistad, L.; Lee, S. *J. Am. Chem. Soc.* **1991**, *113*, 8216.
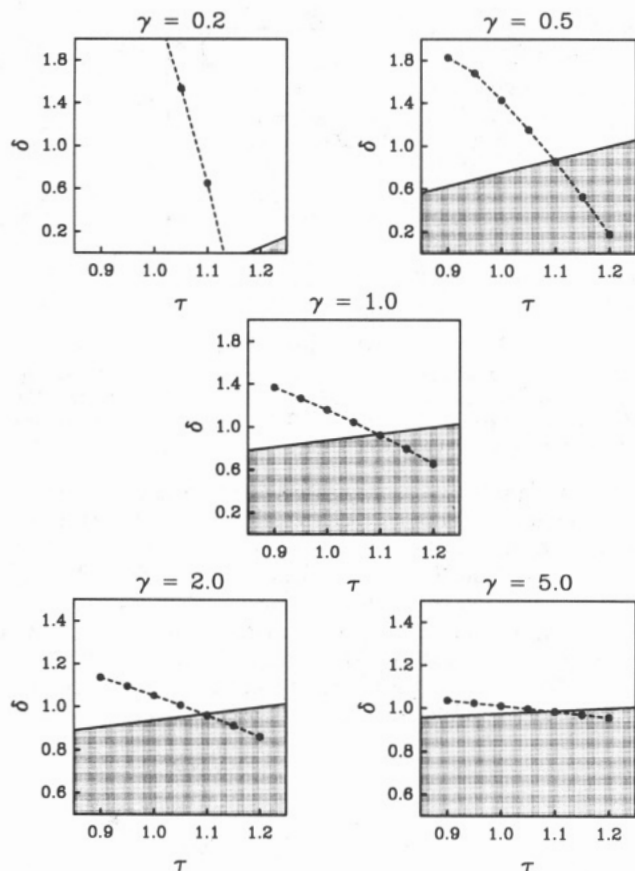
Figure 5. Qualitative variations in the energy difference (ΔE) between d^8 sawhorse and square planar RuH$_4$ units within the two-parameter field δ and τ as defined in the text for different values of γ (see text). Regions of stability for the sawhorse fragment are shaded, and the dashed lines represent the slices along the two energy surfaces for which the two geometries have equal second moments μ_2.

Table 3. Valence Atomic Orbital Energies of Ru Obtained by Charge Iteration for the Various Mg$_2$RuH$_4$ Structures Listed in Table 1[a]

structure	q(Ru)	H_{ss} (eV)	H_{pp} (eV)	H_{dd} (eV)
IIIa	8.350	−7.90	−3.11	−9.76
IIId	8.441	−7.78	−2.74	−9.62
IIIe	8.444	−7.78	−2.72	−9.57
IVa	8.682	−7.19	−2.12	−8.59
IVe	8.673	−7.20	−2.13	−8.62

[a] q(Ru) values are calculated using the AO energy parameters for Ru from **IIIe**.

these RuH$_4$ fragments. The energy of these orbitals is thus exactly Δ(X).

Figure 5, therefore, points out why the sawhorse arrangement is favored for low-oxidation-state d^8 metals, like Ru(0) and Os(O). In this case, Δ(X) will be large (γ is also large), and the effects of charge transfer will quickly favor the C_{2v} geometry. When the potential for valence electrons increases by going to higher oxidation states, as in Rh(I) and Pt(II) (the metals are also more electronegative), smaller γ values occur, and metal–ligand charge transfer will not sufficiently shift δ to regions away from the square planar geometry.

Charge iteration of the Ru parameters for several structural modifications with stoichiometry Mg$_2$RuH$_4$ have shown that the atomic orbital energy parameters depend greatly on the local RuH$_4$ coordination geometry but are rather insensitive to the occurrence of Ru–Ru bonding. Table 3 lists the resulting energy parameters for structures **IIIa**, **IIId**, **IIIe**, **IVa**, and **IVe** along with the Mulliken population of Ru, which was obtained by using the AO parameters from structure **IIIe**. When the difference in Ru populations is approximately 0.2 unit of electronic charge, the energies of the Ru 4d orbitals differ by nearly 0.9 eV; the square planar system gives higher valence atomic orbital energies at Ru. The sawhorse configuration, therefore, gains a lot of electronic energy through population of the three R–H σ nonbonding orbitals.

The dashed lines in Figure 5 correspond to the section of the two intersecting energy surfaces which maintain equal second moments between the two structures. This additional restriction results in specific values of τ for which the sawhorse geometry is preferred. When second-moment scaling is applied, the range of allowed values of τ for stability of the C_{2v} fragment increases as γ increases. This solidifies our conclusion that the angular structure prefers low-oxidation-state d^8 metals. This results also suggests that the square planar geometry for these metals may be stabilized under pressure.

Na$_2$PtH$_4$ vs K$_2$PtCl$_4$

At this point, we wish to discuss briefly the difference in the arrangements of square planar [PtX$_4$]$^{2-}$ complexes found in the structures of Na$_2$PtH$_4$[7] (**IVa**) and K$_2$PtCl$_4$[30] (**IVe**). Previous seminal treatments[9,31] of orbital interactions in the solid state have examined the tetracyanoplatinate chains in K$_2$[Pt(CN)$_4$]·3H$_2$O as well as in the model polymer $^1_\infty$[PtH$_4$]$^{2-}$. Although van der Waals attractions between the closed-shell square planar units as well as hydrogen bonding cannot be excluded, both treatments point out the contribution of an orbital interaction, i.e., bonding between adjacent Pt atoms that involves the mixing of the Pt z^2 and z bands. Both the small z^2–z overlap ($S = 0.042$ for d(Pt–Pt) = 3.40 Å) and the large energetic mismatch between these two orbitals account for a relatively weak interaction. Most of the orbital mixing affecting the occupied levels takes place at the top of the z^2 band. The result of this dp hybridization is to reduce the antibonding component of the z^2–z^2 interaction.

value of γ, the sawhorse geometry requires $\delta < 1$ for all physically reasonable values of τ ($0.9 \leq \tau \leq 1.2$ corresponds to a range d(Ru–H) ± 0.1 Å). For large γ, δ need only be slightly less than 1 for stability of the C_{2v} fragment whereas, for small δ, this region of stability is more restricted. What does $\delta < 1$ physically mean? If we assume the same values for the H 1s AO energies in the two systems, then the Ru 4d AO energies should adopt lower values when the coordination has C_{2v} point symmetry than when it is square planar.

Valence-state ionization potentials, which are used to evaluate orbital energies,[29] are sensitive to the charge of an atom in a molecular or solid-state complex.[18] These values show quadratic behavior with respect to charge and increase as the negative charge on an atom increases. Our Mulliken population results (Table 2) obtain greater negative charge at the metal in square planar coordination. Therefore, we expected $\Delta(D_{4h}) > \Delta(C_{2v})$, or $\delta < 1$. We can visualize these different Ru 4d AO energies as coming from a zeroth-order ligand field effect derived from electron transfer between metal and ligands. The splitting of these energy levels is then governed by the symmetry of the coordination environment.

Nevertheless, how do the values Δ(X) affect the relative energies of these two moieties? Both the sawhorse and square planar geometries may be derived from the octahedron by respectively removing two *cis* and *trans* ligands. Since H offers no valence AO's that can engage in Ru–H π overlap, the octahedron's σ nonbonding t_{2g} orbitals remain nonbonding and degenerate in

(29) McGlynn, S. P.; Vanquickenborne, L. G.; Kinoshita, M.; Carroll, D. G. *Introduction to Applied Quantum Chemistry*; Holt, Rinehart & Winston: New York, 1972.

(30) Kukina, G. A. *Zh. Strukt. Khim.* **1962**, *3*, 474.
(31) Hoffmann, R. *Solids and Surfaces: A Chemist's View of Bonding in Extended Structures*; VCH Publishers, Inc.: New York, 1998.

Calculations on a quasi-infinite chain of $[PtH_4]^{2-}$ units (as in **IIe**) reveal that this orbital mixing occurs but is extremely small and gives a slightly negative overlap population (p(Pt–Pt) = –0.002) between adjacent Pt atoms. These chains are not realized in any of the A_2 PtH$_4$ structures where A is an alkali metal.[3b] K_2PtCl_4, on the other hand, exhibits this direct stacking of square planar complexes with d(Pt–Pt) = 4.10 Å (p(Pt–Pt) = 0.000) and forms by precipitation from aqueous solution![32] Nevertheless, we can identify this type of chain in Li_3RhH_4 with very weakly interacting square planar Rh centers (d(Rh–Rh) = 3.881 Å).[33] The calculated Rh–Rh overlap population in this system is only 0.001. In fact, the arrangement of RhH$_4$ complexes gives a distorted body-centered tetragonal cell (as in Na_2PtH_4), and the shift toward orthorhombic symmetry occurs largely due to the distribution of Li atoms. Using this description, the Li$_3$Rh partial structure may also arise from an ordered defect variant of the MoNi$_4$ structure type (cI10).[34]

We contend, therefore, that the absence of chain formation in A_2PtH_4 lies in the nature of the high-temperature synthesis of these phases, since a solid–solid phase transformation occurs upon cooling.[7,35] Rapid movement of the PtH$_4$ moieties in Na_2PtH_4 at temperatures above 573 K leads to the antifluorite arrangement of cations (A^+) and anions ($[PtH_4]^{2-}$). Not only is there a large Madelung component to the total energy, but also the elctrostatic and nonbonded orbital repulsions between H atoms on different complexes are minimized within the antifluorite structure. When the sample is cooled below the transition temperature, diffusion of either the cations or anions is severely restricted and the Na_2-PtH$_4$ structure type evolves. It is conceivable that similar phenomena involving the RhH$_4$ units is present in Li_3RhH_4 and that the relatively "short" Rh–Rh separation of 3.881 Å arises from polar covalent interactions between Li and H. However, there is no experimental evidence for any transformation in Li$_3$-RhH$_4$.

At this time, we are unable to accurately evaluate van der Waals forces between the square planar moieties, but the nearly negligible overlap populations indicate that these forces may be more significant than the orbital interactions. Mulliken populations at Pt in both $[PtH_4]^{2-}$ and $[PtCl_4]^{2-}$ are 10.356 and 9.143, while the corresponding z^2 values are 1.922 and 1.949, respectively. Thus, according to the London expression for the van der Waals energy from a dipole–dipole potential,[36] the larger z^2 component in the HOMO for the chloro complex as well as the Cl 3p orbital contributions will allow greater van der Waals attractions between $[PtCl_4]^{2-}$ units than between $[PtH_4]^{2-}$.

Mg_3RuH_3: Is There Ru–Ru Bonding?

As a last example, we consider Mg_3RuH_3.[12] This compound contains T-shaped RuH$_3$ units that are directly connected via a long Ru–Ru bond distance of 3.310 Å (see **3**). If we treat Mg in the usual way, then we find Ru(3–) and an effective configuration of $4d^{10}5s^1$! Furthermore, using this counting scheme, there are 17 valence electrons assigned to each T-shaped complex, and only through a Ru–Ru single bond will the transition metal center adopt the 18-electron count. There is a set of d^9 dimers of T-shaped fragments with direct metal–metal bonds. $Ni_2(CN)_6^{4-}$ and $Pd_2(CNCH_3)_6^{2+}$ are two examples, but they are
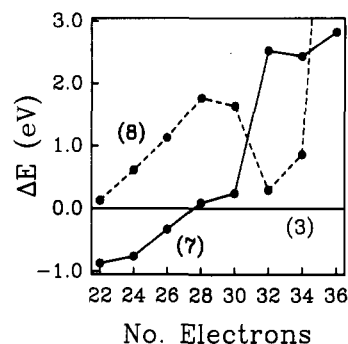

Figure 6. Energy difference curves between three models of Ru_2H_6: solid line, square planar dimer **7**; dashed line, tetrahedral dimer **8**. The reference geometry is the dimer of T-fragments (**3**). Lowest line corresponds to most stable geometry.

not planar;[37] the two T-fragments are rotated by nearly 90° relative to each other. Extended Hückel MO calculations trace this effect to steric repulsion between the ligands. These are 16-electron metal centers, including a formal metal–metal single bond. The electron count and geometry are typical for Ni(II) and Pd(II) chemistry. Two other M_2L_6 geometries are also common for d^8–d^{10} metals: "square planar" dimers (**7**) and "tetrahedral" dimers (**8**), whose chemical bonding and correlations between structure and electronic structure have been analyzed in detail.[38]

7   8
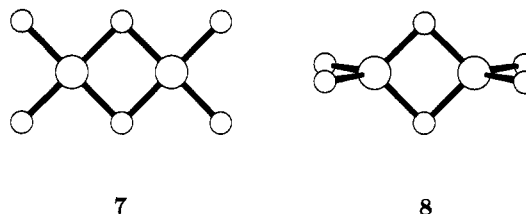
Charge iteration produces to obtain corrected valence-state orbital energies of Ru in Mg_3RuH_3 lead to significant shifts from the ones determined for Mg_2RuH_4, and we have adopted these energies for analysis of its electronic structure (H_{ss} = –6.30 eV, H_{pp} = –1.26 eV, H_{dd} = –7.31 eV).

We begin by comparing the three common geometries for an M_2L_6 moiety: in this case, $Ru_2H_6^{n-}$. In an attempt to overcome the coordination number problem,[28] the energy difference curves in Figure 6 were evaluated using second-moment scaling[28] via the Ru–H interactions. In this case, $\sum S_{Ru-H}^2$ is the same constant value for each structure, in which the summation runs over all valence orbitals. Since Ru is four-coordinate in **7** and **8**, the Ru–H distance is larger than that in the T-shaped geometry. For d^8 configurations and beyond ($n \geq 28$ electrons), the observed structure also gives the lowest total energy. There is also no strong barrier to rotation about the Ru–Ru bond, unlike the case of previous calculations on $Ni_2(CN)_6^{4-}$. This is consistent with the smaller nature of H compared to CN⁻. According to the MO diagram of $Ru_2H_6^{12-}$, all d orbitals are occupied, and the HOMO has Ru–Ru pπ–pπ bonding character which is completely Ru–H nonbonding. The Ru–Ru overlap population of 0.055 favors a significant attractive interaction, yet a distance of 3.331 Å is rather long and a local Ru configuration of $d^{10}p$ is not an appealing conclusion. Thus, what role does Mg play in the electronic structure and chemical bonding in Mg_3RuH_3?

There are two crystallographically inequivalent Mg atoms in the structure of Mg_3RuH_3. According to the labels chosen by

(32) Dickinson, R. G. *J. Am. Chem. Soc.* **1922**, *44*, 2404.

(33) Bronger, W.; Müller, P.; Kowalczyk, J.; Auffermann, G. *J. Alloys Comp.* **1991**, *176*, 263.

(34) Villars, P.; Calvert, L. D. *Pearson's Handbook of Crystallographic Data for Intermetallic Phases*; American Society for Metals: Metals Park, OH, 1985.

(35) (a) Bronger, W.; Auffermann, G.; Müller, P. *J. Less Common Met.* **1986**, *116*, 9. (b) Bronger, W.; Auffermann, G.; Müller, P. *J. Less Common Met.* **1988**, *142*, 243.

(36) Seitz, F. *The Modern Theory of Solids*; Dover Publications, Inc.: New York, 1987.

(37) Schäfer, H.; Eisenmann, B.; Müller, W. *Angew. Chem., Int. Ed. Engl.* **1973**, *12*, 694.

(38) (a) Jarchow, O. *Z. Anorg. Allg. Chem.* **1971**, *383*, 40; *Z. Kristallogr., Kristallgeom., Kristallphys., Kristallchem.* **1973**, *136*, 122. Jarchow, O.; Schulz, H.; Nast, R. *Angew. Chem.* **1970**, *82*, 43. (b) Doonan, D. J.; Bach, A. L.; Goldberg, S. Z.; Eisenberg, R.; Miller, J. S. *J. Am. Chem. Soc.* **1975**, *97*, 1961. Goldberg, S. Z.; Eisenberg, R. *Inorg. Chem.* **1976**, *15*, 535.
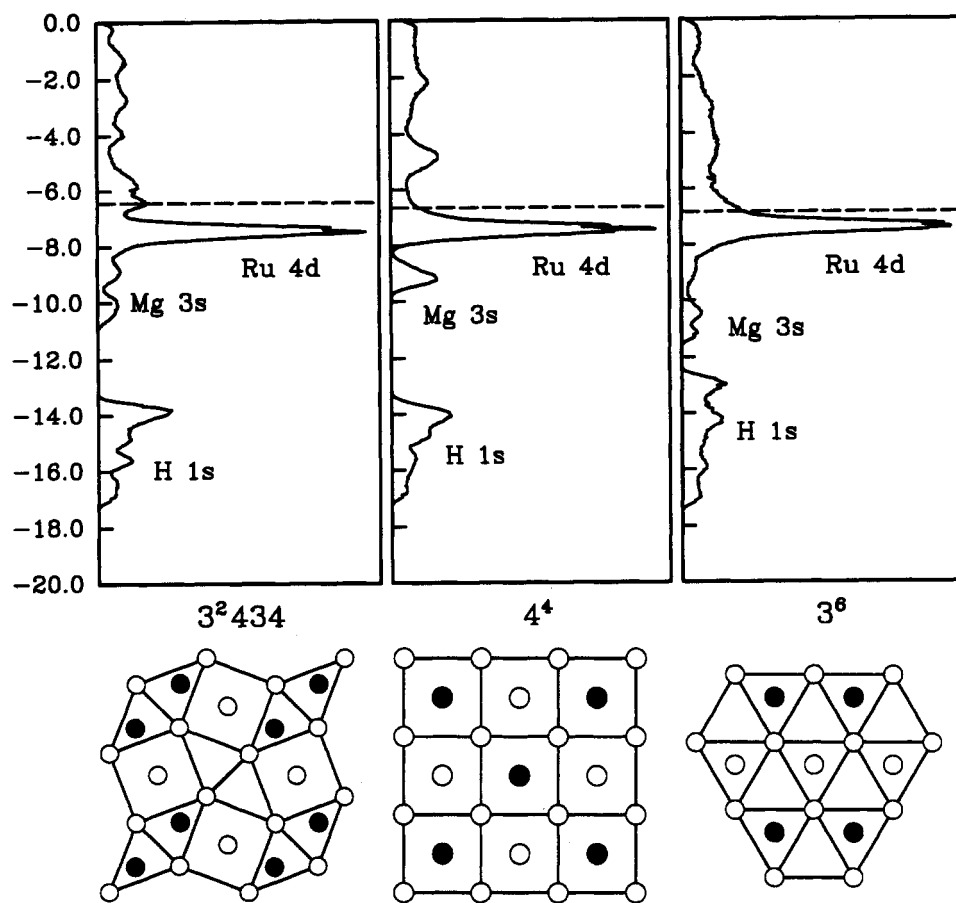
Figure 7. Total DOS for different structural variants of Mg_3RuH_3: left, 3^2434 net of Mg atoms (observed structure); center, 4^4 net of Mg atoms; right, 3^6 net of Mg atoms. The structural models are depicted below each corresponding DOS diagram (only Mg and Ru sites are shown; Ru sites are shaded).

Table 4. Computational Results from Various Structural Models for Mg_3RuH_3[a]

	3^2434	4^4	3^6
energy (eV)	0.000	1.151	0.401
$q(Ru)$	8.146	8.556	8.136
$q(H)$	1.572 (2×)	1.546 (2×)	1.616 (2×)
	1.517 (1×)	1.545 (1×)	1.582 (1×)
$q(Mg)$	1.501 (1×)	1.310 (1×)	1.421 (1×)
	1.347 (2×)	1.248 (2×)	1.313 (2×)
$\langle p(Ru-Ru)\rangle$	0.008 ($^1/_2$)		
$\langle p(Ru-H)\rangle$	0.082 (3)	0.167 (3)	0.190 (3)
$\langle p(Mg-H)\rangle$	0.154 (9)	0.177 (4)	0.123 (7)
$\langle p(Mg-Mg)\rangle$	0.098 (12)	0.112 (10)	0.186 (6)
$\langle p(Mg-Ru)\rangle$	0.027 (8)	0.005 (10)	0.033 (6)

[a] These models are depicted in Figure 7. Numbers in parentheses next to the overlap populations indicate the number of such bonds per formula unit.

Bonhomme et al.,[12] the arrangement of Mg2 atoms is an intermediate between simple cubic packing and simple hexagonal packing. In fact, the Mg2 atoms form slightly puckered 3^2434 nets that are stacked in an eclipsed fashion. The Mg1 atoms center cubic interstices and Ru atoms occupy the center of trigonal prisms. Thus, the environment of Mg1 atoms mimics body-centered-cubic packing while the surrounding of the Ru sites resembles hexagonally closest packing. Since these trigonal prismatic sites share a rectangular face, the questiotn arises concerning the importance of Ru–Ru bonding for stabilizing this structure.

Figure 7 shows how the total densities of states compare for the observed Mg_3RuH_3 structure (3^2434 nets of Mg) with two hypothetical variants based upon body-centered-cubic packing (4^4 nets of Mg) and simple hexagonal packing (3^6 nets of Mg).
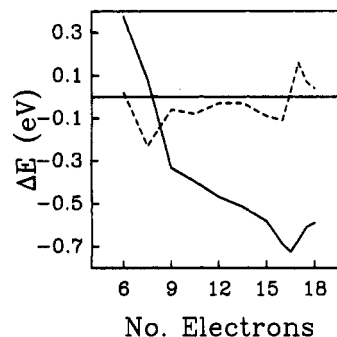

Figure 8. Differences in the total energies (solid) and Fermi levels (dashed) for the observed (**3**) and hypothetical (**9**) structures of Mg_3RuH_3. $\Delta E < 0$ favors the observed structure.

Both alternatives have no Ru–Ru contacts closer than 5.00 Å. These models were set to have the same volume per formula unit as the observed structure and are illustrated along with the DOS curves in Figure 7. The strong peaks just above –8.0 eV are predominantly Ru 4d orbitals and indicate that the Ru–Ru interaction is relatively weak in this compound. The calculated Ru–Ru overlap population of 0.007 further confirms this observation. The relative total energies agree with observation (see Table 4), but the greatest effects in the DOS curves occur at the top of the hydrogen band between –14.0 and –12.0 eV as well as the spectral region between –12.0 and –8.0 eV. In the 3^6 case, short H···H nonbonded contacts result in a broadening of the H band by raising the top of this band through antibonding H···H interactions. On the other hand, there are also stronger Mg–Mg and Mg–Ru interactions. The bottom of the conduction band has significant Mg 3s character. This band is not very dispersive in the 4^4 case. Thus, the energetic stabilization of the
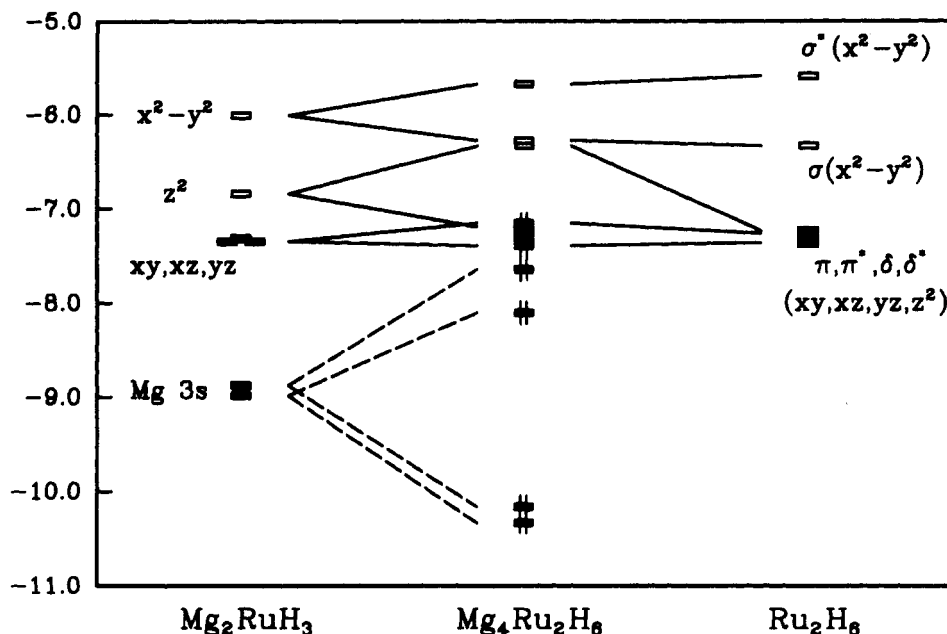
Figure 9. MO correlation diagrams: left, evolution from isolated Mg_2RuH_3 fragments (T-shaped RuH_3) to the dimer $Mg_4Ru_2H_6$; right, correlation between an isolated planar Ru_2H_6 unit and a similar fragment with four capping Mg atoms. Ru–Ru orbital overlap is labeled in the right-hand section, and the occupied levels are set according to the Fermi level of Mg_3RuH_3.
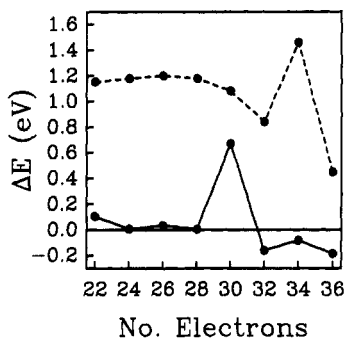

No. Electrons

Figure 10. Solid line: Energy difference curve (eV) between isolated T-shaped RuH_3 units and the dimer Ru_2H_6. Dashed line: Energy difference between monomeric Mg_2RuH_3 units and the corresponding dimer $Mg_4Ru_2H_6$. Positive values occur when the dimers are more stable; negative values occur when isolated monomers are more stable.

intermediate $3^24 34$ (observed) case, at least from the point of view of our DOS curves, arises because there is both weaker H⋯H nonbonded orbital overlap and significant Mg–Ru orbital interactions. Overlap populations for various contacts are listed as well in Table 4.

As Figure 7 illustrates, only half of the pairs of trigonal prismatic sites within a single (001) layer are occupied with Ru atoms. The 4_2 screw axes in Mg_3RuH_3 arise by alternating the occupation of these sites from one layer to the next. Thus, another model to investigate the importance of Ru–Ru bonding is to eliminate the pairs but to adopt a pattern as shown in **9**. The observed
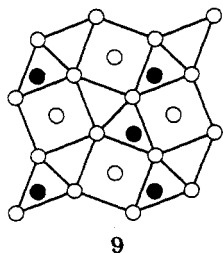
9

structure wins by nearly 1.3 eV per Ru–Ru pair. Figure 8, which plots both the energy differences and the difference in Fermi

energies for these two models, points out that a large driving force for the observed structure occurs via Mg–Ru interactions and that Ru–Ru bonding has a secondary influence. The sharp drop in both ΔE and ΔE_F values between 6 and 9 valence electrons per formula unit occurs when the DOS for both structures are largely Mg 3s. From 9 to approximately 17 electrons, both Ru–Ru and Ru–Mg ($d\pi$–$p\pi$) interactions contribute to the lower values for the observed structure. However, above 17 electrons, Ru–Ru antibonding interactions produce the sharp increases in ΔE and ΔE_F.

How should we assign electrons in this system? In MgH_2, Mulliken populations evaluated from extended Hückel calculations give $q(Mg) = 0.85$, i.e. $Mg^{1.15+}$ $(H^{0.575-})_2$. However, in Mg_3RuH_3, we find $q(Mg1) = 1.50$ and $q(Mg2) = 1.35$. Now, Mulliken populations generally overestimate the amount of electron density that builds up on electropositive elements, but the trend here is clear. Mg, and especially Mg1, atoms are involved in some degree of metallic bonding with Ru as well as other Mg atoms in this compound. Figure 9 illustrates how four Mg atoms sitting in a plane perpendicular to the plane of a $H_3Ru–RuH_3$ dimer, as found for the Mg1 atoms in Mg_3RuH_3, alter the pattern of MO's of this Ru_2H_6 fragment. There are low-lying hydrogen-centered orbitals (at energies near −14.0 eV) that are not shown. In Ru_2H_6, eight virtually Ru–H nonbonding orbitals near −7.3 eV are followed by the Ru–Ru σ and σ^* combinations of Ru–H antibonding $x^2 - y^2$ orbitals. With Mg atoms included in the xz plane, one of the eight Ru–H nonbonding orbitals up in energy: the Ru–Ru antibonding combination of z^2 orbitals. We set the HOMO of this model according to the position of the Fermi level in Mg_3RuH_3 and find that it belongs to the set of Ru–H nonbonding orbitals with Ru–Ru π^* character (yz–yz) and leads to a Ru–Ru overlap population of −0.006. Therefore, the three highest lying d orbitals of the Ru_2H_6 fragment remain unoccupied. However, due to significant contributions from Ru 5s and 5p orbitals in the occupied bands, a d^7 configuration does not lead to Ru(I) in this system.

Energy difference curves in Figure 10 compare the energy of two isolated monomers with the dimer and indicate that maximum stabilization in the electronic energy occurs for 17 electrons per monomer when Mg atoms are included but for 15 electrons when they are not. Thus, Mg orbitals play a critical role in the electronic and subsequent structural stability of Mg_3RuH_3.

Table 5. Atomic Parameters Used in the Extended Hückel Calculations[a]

atom	orbital	H_{ii} (eV)	ζ_1	C_1	ζ_2	C_2
H	1s	−13.60	1.30			
Mg	3s	−9.00	1.10			
	3p	−4.50	1.10			
Ru	5s	−7.78	2.08			
	5p	−2.72	2.04			
	4d	−9.57	5.38	0.5573	2.30	0.6642
Pt	6s	−9.08	2.55			
	6p	−5.48	2.55			
	5d	−12.59	6.01	0.6334	2.70	0.5513

[a] Double-ζ functions are used for the transition metals.

In terms of local chemical bonding, we can now rationalize in a simple way the preference for the observed structure over structure **9**. A subtle observation of the coordination geometry of Mg1 by Ru reveals two-coordination in the xy plane. In the observed structure, this Ru–Mg–Ru unit is linear, whereas in the hypothetical alternative it is bent. According to Figure 9, the primary orbital interactions are z^2–s–z^2, and this system will have four electrons (two from the 3s orbital plus one each from the Ru z^2 orbitals). This three-center four-electron problem has been extensively studied[9] and gives the linear geometry, as observed around Mg1 in Mg_3RuH_3.

Summary

The new ternary magnesium ruthenium hydrides have provided challenges in trying to correlate electronic structure with observed geometries. Our results suggest that Mg is playing a role beyond a classical cation, as typically observed for alkaline earth elements in numerous inorganic solids known as Zintl phases.[39] Valence orbitals of Mg are involved in covalent interactions with Ru as well as H, which lead to the electronic stability and apparent metallic character of these ternary compounds. Furthermore, the special feature of H as a ligand, i.e., no valence p orbitals, provides increased electron density at the transition metal and pushes up the valence-state orbital energies of Ru. This, coupled with Ru–Ru interactions, gives rise to many of the fascinating compounds, and, of course, structures, in this system.

Appendix

All electronic structure calculations were of the extended Hückel tight-binding type.[40] Observed structures of Mg_2RuH_4,[8] Na_2PtH_4,[5] Li_3RhH_4,[33] and Mg_3RuH_3[9] were utilized. Model and hypothetical structures were constrained to have the same formula unit volumes and identical M–H distances (M = Ru, Rh, Pt) compared to those of the observed structures. DOS and COOP curves were evaluated using special k-point sets,[41] and tight-binding overlaps were included within two neighboring unit cells along every translation vector. Atomic orbital parameters[42] and charge iteration parameters[43] for Ru were taken from standard sources and are listed Table 5.

(39) Summerville, R. H.; Hoffmann, R. *J. Am. Chem. Soc.* **1976**, *98*, 7240.
(40) (a) Whangbo, M.-H.; Hoffmann, R. *J. Am. Chem. Soc.* **1978**, *100*, 6093. (b) Ammeter, J.; Bürgi, H.-B.; Thibeault, J. C.; Hoffmann, R. *J. Am. Chem. Soc.* **1978**, *100*, 3686.
(41) Chadi, D. J.; Cohen, M. L. *Phys. Rev. B* **1973**, *8*, 5747.
(42) (a) Clementi, E.; Roetti, C. *At. Data Nucl. Data Tables* **1974**, *14*, 177. (b) Zheng, C.; Hoffmann, R. *Z. Naturforsch.* **1987**, *41B*, 292.
(43) Baranovskii, V. I.; Nikolskii, A. B. *Teor. Eksp. Khim.* **1967**, *3*, 527.